



Application of remote sensing data in gold exploration: targeting hydrothermal alteration using Landsat 8 imagery in northern Portugal

Rui Frutuoso^{1,2} · Alexandre Lima^{1,2} · Ana Cláudia Teodoro^{1,2} 

Received: 30 December 2020 / Accepted: 17 February 2021 / Published online: 8 March 2021
© Saudi Society for Geosciences 2021

Abstract

Mapping hydrothermal alteration minerals and structural lineaments using Landsat 8 multispectral imagery provides valuable information for mineral exploration. In northern Portugal, there are several known gold occurrences, but there is the potential to identify new anomalous areas. Gold mineralization occurs in the form of quartz veins and veinlets associated with hydrothermal alteration halos. Fractures are interpreted as conduits for mineralizing fluids, where the interaction between the wall rock and hydrothermal fluids induces compositional variations. Identifying these features is one of the key indicators for targeting new prospective zones of orogenic gold mineralization in the Boticas–Chaves region. Remote sensing image processing methods such as band combinations, band ratios, and principal component analysis (PCA) were implemented to the visible, near-infrared, and shortwave infrared bands of Landsat 8. The results of this investigation demonstrate the capability of the applied imagery enhancement methods in distinguishing different features and identifying hydrothermally altered rocks. Selective PCA proved to be the most effective and reliable method to identify iron oxides and hydroxyl-bearing minerals, compared to other methods, where a simple imagery analysis has a strong influence of noise and is more challenging to interpret. Enhanced imagery allowed the identification of physiographic characteristics and extracted structural features. The combination of mapped hydrothermal alteration minerals and extracted structural features allowed us to predict potential areas for the mineralization occurrence. This investigation proves that remote sensing can be a cost-efficient and time-saving technique for mineral exploration, and its application in new areas can accurately map hydrothermal alteration and outline potential new exploration targets.

Keywords Remote sensing · Landsat · Hydrothermal alteration · Gold · Mineral exploration

Introduction

Geological remote sensing has proven to be an effective and important tool for locating mineral deposits and identifying mineral associations through spectral anomalies (Sabins 1999; Rajesh 2004; Robert et al. 2007; van der Meer et al. 2012; Cardoso-Fernandes et al. 2019). Remote sensing is a powerful technique for recognizing hydrothermally altered rocks, structures, lineaments, lithological units, vegetation, and other valuable information for geologists (Goetz et al. 1982; Sabins 1999; Drury 2001; Nikolakopoulos et al. 2008; Goetz 2009; Mielke et al. 2014; Cudahy 2016; Pour et al. 2018a, Pour et al. 2018b; Bolouki et al. 2020; Mahboob et al. 2019; Pour et al. 2019; Beygi et al. 2020; Cardoso-Fernandes et al. 2020a; Cardoso-Fernandes et al. 2020b; Traore et al. 2020; Takodjou Wambo et al. 2020). Regional mapping of exposed altered rocks with remote sensing supports exploration teams, helping to identify

Responsible Editor: Biswajeet Pradhan

✉ Ana Cláudia Teodoro
amteodoro@fc.up.pt

Rui Frutuoso
rui.frutuoso@fc.up.pt

Alexandre Lima
allima@fc.up.pt

¹ Department of Geosciences, Environment and Land Planning, Faculty of Sciences, University of Porto, Rua Campo Alegre, 4169-007 Porto, Portugal

² Institute of Earth Sciences (ICT), Pole of University of Porto, 4169-007 Porto, Portugal

target exploration areas (Sabins 1999; Robert et al. 2007; Cudahy 2016; Pour et al. 2018b; Bolouki et al. 2020; Booysen et al. 2019; Eldosouky et al. 2020; Pour et al. 2019; Beygi et al. 2020; Sekandari et al. 2020; Traore et al. 2020; Takodjou Wambo et al. 2020). Since the 1970s, multispectral remote sensing imagery has been used for regional mineral exploration, such as images from NASA's Landsat. The spectral signatures of minerals and mineral assemblages formed by hydrothermal alteration are used to identify outflows of hydrothermal systems, which can support the recognition of mineralized zones (Sabins 1999; Rajesh 2004; Moradi et al. 2014). The spectral signatures of minerals and rocks are based on work by Hunt (1977) and Salisbury et al. (1989), who measured in the laboratory the spectra of several different minerals and rocks. Afterwards, a number of techniques and analysis methods were developed to process satellite imagery and recognize hydrothermal alteration areas.

Since then, several published studies proved the potential for remote sensing in mapping hydrothermally altered rocks. Rowan et al. (1977) identified hydrothermally altered rocks using Landsat Multispectral Scanner (MSS) bands in south-central Nevada. Moulton and Ridd (1990) used Landsat Thematic Mapper imagery integrated with geophysical data to identify hydrothermal alterations in the east Tintic mining district of Utah. Crósta et al. (2003) mapped key alteration zones related to epithermal gold deposits in Patagonia, using Advanced Spaceborne Thermal Emission and Reflection (ASTER) imagery. Nikolakopoulos et al. (2008) performed a comparison of hyperspectral data from EO-1 Hyperion with multispectral data from the EO-1 Advanced Land Imager and Landsat 7 ETM⁺ for mineral mapping in Milos Island, Greece. Zoheir and Emam (2012) mapped gold exploration targets in the Eastern Desert, Egypt, using ASTER and Landsat Enhanced Thematic Mapper Plus (ETM+) imagery. Pour and Hashim (2015) mapped hydrothermal alteration areas and lithological units in the Sar Chshemeh copper mining district of southeast Iran using Landsat 8 imagery. Safari et al. (2017) used Landsat 8 data to map hydrothermal alteration zones associated with porphyry copper and epithermal gold mineralization in the Shahr-r-Babak region of Iran. Pour et al. (2018b) used Landsat 8, ASTER, and WorldView-3 multispectral data to map hydrothermally altered areas associated with copper-gold mineralization in Inglefield Land, Northwest Greenland. Zoheir et al. (2019) explained regional structural control of orogenic gold mineralization in the Barramiya-Mueilha sector of Egypt using Sentinel-1 and Sentinel-2, Phased Array type L-band Synthetic Aperture Radar (PALSAR), and ASTER imagery to extract structural features and highlight hydrothermally altered zones. Takodjou Wambo et al. (2020) generate mineral prospectivity maps for gold mineralization in a sub-tropical region, eastern Cameroon, using Landsat 8 and ASTER imagery analysis to identify hydrothermal alteration zones. Sekandari et al. (2020)

analyzed Landsat 8, Sentinel-2, ASTER, and WorldView-3 spectral data for detailed mapping of alteration zones, lithological units, and structural features associated with carbonate-hosted Pb-Zn mineralization in the Central Iranian Terrane. Most of these geologically remote sensing studies for mineral exploration were done in arid and semi-arid regions, where the acquisition of spectral reflectance data from rocks and soils is not so exposed to spectral noise from urbanized areas and agricultural lands or covered by vegetation. These remote sensing methodologies have not been broadly used in Portugal, where only a few investigations have been produced in recent years. Pereira et al. (2012) and Cardoso-Fernandes et al. (2018, 2019, 2020a, b) applied different multi sensor data to detect lithium-bearing pegmatites, and Lima et al. (2014b) and Manuel et al. (2017) used remote sensing methods in order to map structural features and alteration minerals associated with gold mineralization, in Mirandela and Góis region, respectively. The present investigation selected an area in Boticas-Chaves region, northern Portugal with a long history of gold exploration and several known occurrences, characterized by anorogenic gold system generally associated with hydrothermally altered areas. Gold mineralization is hosted in quartz veins within granites and is believed that it is controlled by a large-scale regional fault, the Régua-Verín Fault, a structural feature associated with many large-scale orogenic gold deposits located in the district (Fuertes-Fuente et al. 2016). Well-established remote sensing methods, such as band combinations, band ratios, and principal component analysis (PCA) applied to multispectral visible and near-infrared (VNIR) and shortwave infrared (SWIR) spectral bands, allow mapping iron oxides and hydroxyl-bearing minerals. In this study, Landsat 8 data were used to detailedly map the different hydrothermal alteration minerals and extract structural features. This information allowed to identify highly potential areas of gold occurrence, defining exploration targets, bypassing time-consuming field reconnaissance, and avoiding geochemical and geophysical studies in uninteresting areas for mineral occurrence.

Study area

The study area is located within the Trás-os-Montes region, northern Portugal. This area covers approximately 690 km² of Boticas and Chaves counties, and is bounded on the north by the border with Galicia, Spain, and on the east by a NNE-SW striking valley known as the Régua-Verín Fault. The latter extends 200 km from Penacova to Verín and represents a dextral active fault system associated with several thermal events along its strike (Cabral 1995; Lourenço et al. 2002; Fuertes-Fuente et al. 2016). Toward the west, it is bordered by the Rabagão reservoir and Barroso Mountain.

Several archeological occurrences from the pre-Roman era have been found in this area (Martins 2005; Lima et al. 2014a). Mining activity was ongoing during the Roman presence in this region (Martins 2005; Lima et al. 2011; Lima et al. 2014a). These ancient mines comprise open pits and rare underground works (Matias 2004; Martins 2005; Lima et al. 2014a).

Geological setting

The study area is located in the Iberian Massif, the occidental portion of the European Variscan belt. The Iberian Massif consists of four tectonic zones with contrasting characteristics regarding their structure, stratigraphy, metamorphism, and magmatism (Lotze 1945; Julivert et al. 1974; Farias et al. 1987). The Boticas–Chaves region is located within the parautochthonous Galicia Trás-os-Montes Zone (GTMZ), which consists of a west-northwest trending fold–thrust belt overprinting the Central Iberian Zone (Fig. 1). The GTMZ is characterized by a metasedimentary sequence composed of phyllites, micaschists, and quartz greywackes with rare calcsilicate rocks (Farias et al. 1987; Ribeiro et al. 2000; Ribeiro et al. 2003; Ribeiro et al. 2007; Catalán et al. 2007; Noronha et al. 2013). This metasedimentary sequence was intruded by two main Variscan granitoid groups: (i) syn-kinematic two-mica granite (315–310 Ma), which varies from medium-grained to coarse-grained and from equigranular to porphyritic, being fractured and hydrothermally altered (Noronha et al. 2000); and (ii) two-mica to biotite late-kinematic to post-kinematic granite (310–280 Ma), which is controlled by the NNW-SSE trending Régua-Verín regional fault, a major shear structure, mostly accommodating late deformation and bearing evidence of polyphase reactivation (Ferreira et al. 1987; Dias et al. 1998; Noronha et al. 2000).

Gold mineralization

Gold occurrences in northern Portugal show distribution parallel to the Variscan structures, granitic massifs, and late-Variscan fractures, where veins were affected by different phases of deformation that varied from ductile-brittle to brittle (Ferreira et al. 1987; Noronha and Ramos 1993; Dias et al. 1998; Noronha et al. 2000; Noronha et al. 2013). During the Variscan cycle, significant fluid production and circulation were responsible for the ore concentration. These mineralizing fluids have metamorphic and/or magmatic origin, being produced by rock dehydration and mixed with oxidizing meteoric fluids (Noronha et al. 2000). The main channels responsible for fluid circulation consist in large discontinuities that developed during ductile-brittle to brittle phases of deformation with NNW-SSE and NNE-SSW fractures playing an

important role (Noronha et al. 2000). This fracture system controlled intrusion of post-tectonic granites (280–270 Ma) that activated convective circulation of hydrothermal and meteoric fluids. Fluid circulation remobilized pre-existing gold in the Paleozoic metasediments and enhanced its concentration in favorable zones (Noronha et al. 2000). Gold mineralization is related to progressive dilution and cooling of crustal fluids by mixing with meteoric fluids. Gold was deposited in structural and geochemical “traps” as microfractures of sulfides, where it precipitates by electrochemical processes (Noronha et al. 2000).

Noronha and Ramos (1993) proposed four stages of ore formation based on different mineral associations in gold deposits of northern Portugal. The early stage is characterized by the association between oxides and silicates such as rutile, feldspars, cassiterite, and wolframite. A later ferric-arsenic stage is characterized by the association of arsenopyrite, pyrite, pyrrhotite, and bismuthinite. An intermediate stage of cupriferous zinc is characterized by the association of chalcopyrite and sphalerite. Two late stages were (i) lead-antimoniferous with galena and sulphosalts and (ii) antimoniferous with antimony and berthierite. Based on these mineralogical associations, Noronha and Ramos (1993) defined three types of occurrences: (i) As-Fe-Bi-Au-Ag-(W-Mo-Sn-Cu-Pb-Zn), corresponding to a mineralogical association of arsenopyrite-pyrite-bismuth-gold-electrum-(tungstate-cassiterite-stannite-molybdenite-chalcopyrite-sphalerite-galena-sulphosalts); (ii) As-Fe-Pb-Zn-Cu-Au-Ag-(Sb-Cd), corresponding to a mineralogical association of arsenopyrite-pyrite-galena-chalcopyrite-sphalerite-gold-electrum-(sulphosalts); and (iii) a combination of the two.

Fuertes-Fuente et al. (2016) provided a detailed description of mineralization in the Limarinho deposit (Fig. 1), where two gold parageneses were defined. In the first, Bi-Te-(±S), gold occurs as native, along with native-Bi, hedleyite, and joséite-B, in inclusions in sulfides. In the second, (±Cu)Ag-Pb-Bi-S ±Te, gold occurs as electrum in intergranular spaces or fractures or in cavities of sulfides and quartz gangue and comprises (±Cu)Ag-Pb-Bi sulfosalts, Pb-Bi sulfotellurides, and hessite. These authors also proposed two mechanisms for gold mineralization: (i) bismuth melt scavenging gold from a gold-unsaturated hydrothermal fluid (Au-Bi-Te±S paragenesis) and (ii) gold remobilization together with new gold deposition due to sulfur extraction from the hydrothermal fluid during the stage of prevailing sulfide precipitation. These two events of gold precipitation may have enhanced the gold grade in this deposit.

The mineralized structures in the study area consist of quartz veins or veinlets, sometimes in stockwork, striking N20–40°, with a subvertical dip and thickness from 2 up to 20 cm (Cepedal et al. 2013; Fuertes-Fuente et al. 2016). Fuertes-Fuente et al. (2016) described two main stages of mineral deposition in quartz veins followed by successive periods of vein reopening, crosscut by irregular veinlets (stage

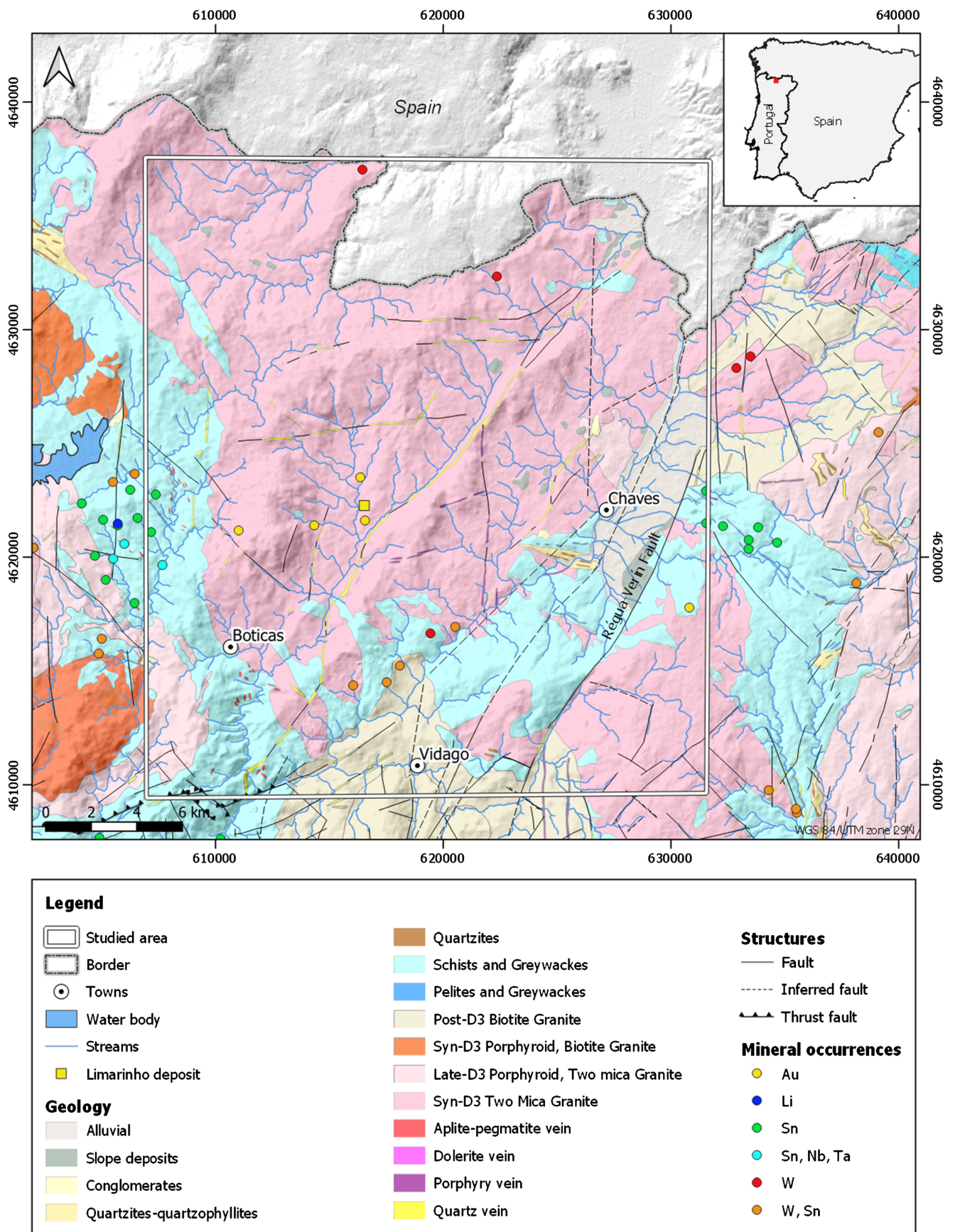


Fig. 1 Geological map of the study area showing mineral occurrences

III). Stage I is characterized by milky quartz and arsenopyrite veins, whereas stage II corresponds to the formation of clear quartz, k-feldspar, chlorite, rutile, arsenopyrite, and pyrite, with galena, chalcopyrite, and sphalerite in minor amounts. Stage III veinlets and cavity fillings comprise vermicular chlorite, sometimes clear euhedral quartz crystals, galena, and pyrite.

Intense vein density zones are accompanied by strong alteration of the wall rocks. This process of hydrothermal alteration is related to the interaction between wall rocks and hydrothermal fluids, including heat and chemical compounds inducing wall rock compositional changes.

Materials and methods

Landsat-8 remote sensing data

In this investigation, Landsat 8 OLI multispectral imagery level 1T (path 204; row 31), acquired on 9 May 2015 under excellent weather conditions (1.24% cloud cover) and image quality, were used to extract mineralogical and structural information in Boticas-Chaves region, Portugal. Landsat 8 is an American satellite launched in 2013 by a collaboration between NASA and the United States Geological Survey (USGS). The eighth satellite of the Landsat program carries 2 instruments onboard: the Operational Land Imager (OLI), which consists of 9 bands with a spectral resolution of 30 m (bands 1–7 and 9) and 15 m for a panchromatic band (band 8), and the Thermal Infrared Sensor (TIRS), which includes 2 thermal bands (bands 10 and 11) collected with 100 m spatial resolution but resampled to 30 m (USGS 2020a).

Data gathered in visible and SWIR regions have particular features for geological applications (Rajesh 2004; Mwaniki et al. 2015; USGS 2020a, b):

- Band 4 (visible: 0.64–0.67 μm): appropriate for discriminating soil and vegetation and delineating soil cover.
- Band 6 (SWIR: 1.57–1.65 μm): for soil and rock discrimination, sensitive to moisture variation in vegetation and soils and to the presence of ferric iron or hematite-rich rocks.
- Band 7 (SWIR: 2.11–2.29 μm): coincides with absorption features caused by hydrous minerals (clay mica, some oxides, and sulfates), making them appear darker, usually used in lithological mapping.

For this study, band 1 (coastal aerosol), band 9 (cirrus), and bands 10 and 11 (TIRS bands) were discarded from the analysis. Thermal bands were not used due to the lower spatial resolution.

Imagery preprocessing

Preprocessing procedures are important to obtain spatially and radiometrically corrected images. Landsat imagery is currently corrected by the USGS EROS Center, with radiometric correction and geometric correction available (USGS 2020a). The data were converted to top of atmosphere (TOA) reflectance using radiometric coefficients (USGS 2020b), where digital numbers (DN) are converted to TOA reflectance representing the ratio of radiation reflected off a surface to the radiation striking it (USGS 2020a). In order to convert TOA reflectance to surface reflectance, the dark object subtraction 1 (DOS1) atmospheric correction was applied. These steps were performed in the QGIS software using the Semi-Automatic Classification Plugin (SCP) (Congedo 2016).

After this, the spatial resolution of images from Landsat 8 bands 2 to 7 was improved through the application of a pan-sharpening algorithm (Brovey transform), in SCP (Congedo 2016). Panchromatic band 8 (15 m) was used in this procedure.

Image processing methods

Image processing methods transform multispectral satellite data into images that enhance geological features in contrast to the background. In this study, enhancement techniques such as band composite, band rationing, and principal component analysis (PCA) were applied to extract spatial and spectral information related to lithology, structure, and hydrothermally altered zones. The overall workflow for the image processing analysis is schematically represented in Fig. 2.

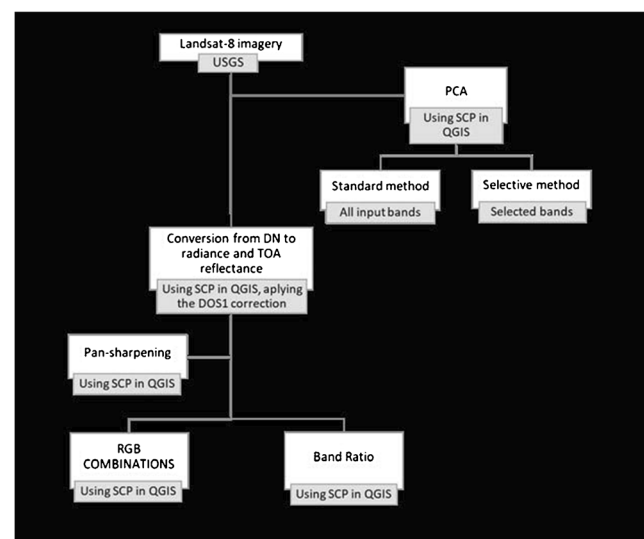


Fig. 2 Schematic diagram of overall workflow

RGB combinations

Landsat imagery is composed of greyscale images that translate spectral bands. A composite of three bands (red, green, and blue) creates a multispectral color image. Different band combinations, based on laboratory spectra of minerals, can be used to enhance geological features (Pour and Hashim 2015). Some well-known RGB combinations for Landsat 8 were tested to identify (i) hydrothermal alteration: RGB 752 and RGB 567 (Pour and Hashim 2015), and RGB 573 (Mia and Fujimitsu 2012); (ii) iron oxides and clay minerals: RGB 257 and RGB 657 (Ali and Pour 2014); and (iii) lithological contrasts: RGB674 (Mwaniki et al. 2015).

Band ratio

Band rationing is a technique whereby one band is divided by another in order to highlight features that cannot be seen in raw bands (Nikolakopoulos et al. 2008; Ali and Pour 2014; Pour and Hashim 2015). The ratios improve contrast and enhance compositional information while suppressing useless information, such as shadowing and topographic surface shadows (Nikolakopoulos et al. 2008; van der Meer et al. 2012; Ali and Pour 2014; Jain et al. 2018; Bolouki et al. 2020; Cardoso-Fernandes et al. 2019; Sekandari et al. 2020).

Considering Landsat 8, minerals such as alunite and clay minerals such as illite, kaolinite, and montmorillonite have distinctive absorption (low reflectance) features at SWIR 2 (2110–2290 nm) and low absorption at SWIR 1 (1570–1650 nm) bands (Sabins 1999), whereas iron oxides and sulfate minerals commonly have strong reflectance near red (640–670 nm) and low reflectance in the blue band (450–510 nm) (Sabins 1999; van der Meer et al. 2012; Ali and Pour 2014; Pour and Hashim 2015). Based on the spectral reflectance and position of the absorption, some authors have proposed band ratios for geological use in order to highlight minerals associated with hydrothermally altered rocks features (Table 1).

An RGB image composed of band ratios will discriminate altered from unaltered ground and highlight areas where concentrations of these minerals occur (Rajesh 2004). Sabins (1999) proposed the RGB combination 4/2, 6/7, and 6/5 for lithological mapping and recognition of hydrothermal alteration zones. Pour

and Hashim (2015) pointed out that RGB composite 4/2, 6/7, and 5 is useful for the identification of lithology, altered rocks, and vegetation. With the same purpose, the Kaufmann ratio (7/5, 5/4, 6/7) was also applied in this work (Mia and Fujimitsu 2012).

Principal component analysis

Principal component analysis (PCA) is a technique used to enhance and separate certain spectral signatures from the background (Gabr et al. 2010; Moradi et al. 2014; Pour et al. 2018b; Bolouki et al. 2020; Sekandari et al. 2020; Takodjou Wambo et al. 2020). PCA is a multivariate statistical technique that selects uncorrelated linear combinations (eigenvector loadings) of variables in such a way that each successively extracted linear combination or principal component (PC) has lower variance (Singh and Harrison 1985; Mia and Fujimitsu 2012). The number of output PCs is the same as the number of input spectral bands. Thus, PCA consists of a linear transformation applied to highly correlated multidimensional data like multispectral imagery, which has a similar visual appearance for different bands, causing data redundancy (high correlation of spectral bands) (Loughlin 1991).

PC analysis can be used in a standard or selective method (Loughlin 1991). For standard analysis, all available spectral bands are used in the input for the PC calculation; in selective analysis, PCA is applied to selected input bands. For enhancement of hydrothermal alteration zones, only the bands with spectral characteristics for iron and hydroxyl-bearing minerals are used (Crósta and Moore 1989; Loughlin 1991; Crósta and Rabelo 1993). An examination of PCA eigenvector loadings can decide which PC image contains more information related to the theoretical spectral signatures of altered minerals (Singh and Harrison 1985; Loughlin 1991).

Results

RGB combinations

Single band combination RGB images were produced to highlight features not distinguished in visible spectral images. A true

Table 1 Tested band ratios for Landsat 8 imagery

Band ratio	Feature	References
4/2	Iron oxides	Sabins (1999), Ali and Pour (2014), Sekandari et al. (2020)
6/7	Alunite and clay minerals	Sabins (1999), Ali and Pour (2014), Pour and Hashim (2015)
6/5	Ferrous minerals	Nikolakopoulos et al. (2008), Mia and Fujimitsu (2012), Ali and Pour (2014)

color image was produced with Landsat 8 visible surface reflectance bands 4, 3, and 2 (red, green, and blue, respectively). This band combination reproduces a natural color image and allows an exploratory analysis of the area, distinguishing rock exposure areas, vegetated areas, water bodies, and urbanized areas. False color images were created using different band combinations. Some of them highlight areas with vegetation or urban areas, like the 543 and 764 combinations. RGB color combination images allocated to near-infrared (band 5) and shortwave infrared (bands 6 and 7) are more appropriate to identify geological and structural features, and more specifically hydrothermally altered rocks. Band combinations 573 and 567 (Fig. 3) better distinguish different features on a regional scale, such as rock exposure, vegetated and urbanized areas, and structural lineaments. In the 573 combination (Fig. 3a), vegetation is shown in red and dark red, urban areas and ploughed fields in light blue and light green, and rock outcrops in green, with alterations in shades of green to light blue. Ploughed fields are shown in the same light blue as some rock outcrops, probably due to soil remobilization exposing clay and iron oxide minerals. In this combination, burned areas are shown as an intense green.

In the 567 combination (Fig. 3b), the vegetation is shown in orange and dark red (different colors correspond to different vegetation types), urban areas and ploughed fields are light blue to blue, and water bodies are black. The rock exposure has a subtle variation between light blue and greenish-blue but lithological

differences are not clear. Alteration minerals, such as clay minerals and iron oxides, are shown in light blue. Bands 6 and 7 (SWIR bands) are useful for soil and rock detection, but different types and densities of vegetation also become clear with these bands. This explains the intense blue areas, corresponding to burned areas.

Band ratio

The band ratio method was also applied to create combination RGB images enhancing hydrothermally altered rocks. The ratio of band 4/band 2 was applied to highlight areas with abundant iron oxide-bearing minerals as brighter pixels (Fig. 4a). The ratio of band 6/band 5 discriminates ferrous minerals in a bright tone. The ratio of band 6/band 7 distinguishes altered rocks containing clays and alunite at bright pixels (Fig. 4b).

Based on the literature, RGB composite images containing band ratios were produced. An image using Sabin's ratio (4/2, 6/7, 6/5) was computed for lithological mapping and identification of hydrothermal alteration zones (Fig. 5a). The ratio 4/2 was used for mapping iron oxides, which are depicted in pink and orange. The ratio 6/7 was used to map clay mineral areas, which are represented in green, but it is also sensitive to moisture variation in vegetation and soils, highlighting vegetation too. The ratio 6/5 shows high reflectance indicative of the presence of ferrous minerals (purple).

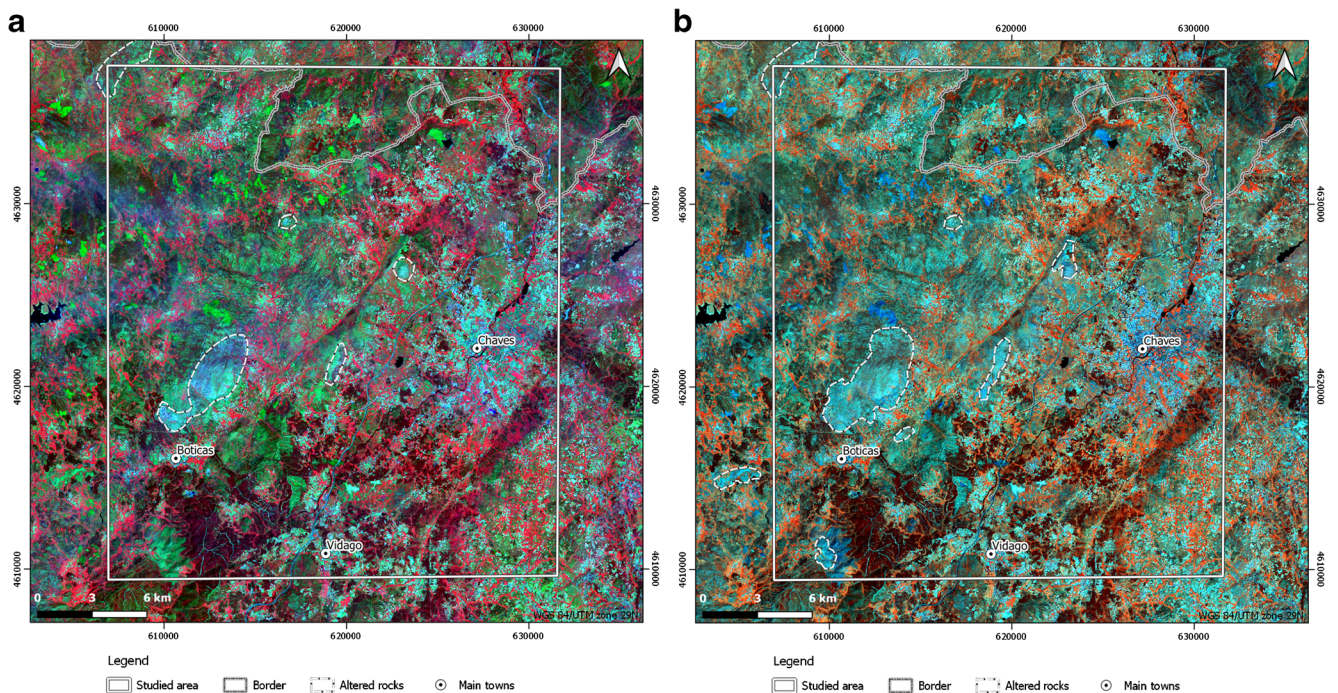


Fig. 3 False color composites enhancing the different spectral signatures in the study area. **a** RGB 573—vegetation is shown in shades of red, urban areas and ploughed fields in light blue to light green, and rock outcrops in shades of green to light blue. The intense light blue color observed in rock outcrops is interpreted as alteration, highlighted with

white dash line. **b** RGB 567—the vegetation appears in shades of orange and dark red, urban areas and ploughed fields in light blue to blue, and rock exposure in shades of greenish-blue to light blue color. The light blue color in rock exposure can be attributed to the alteration minerals within these lithological units (highlighted in white dash lines)

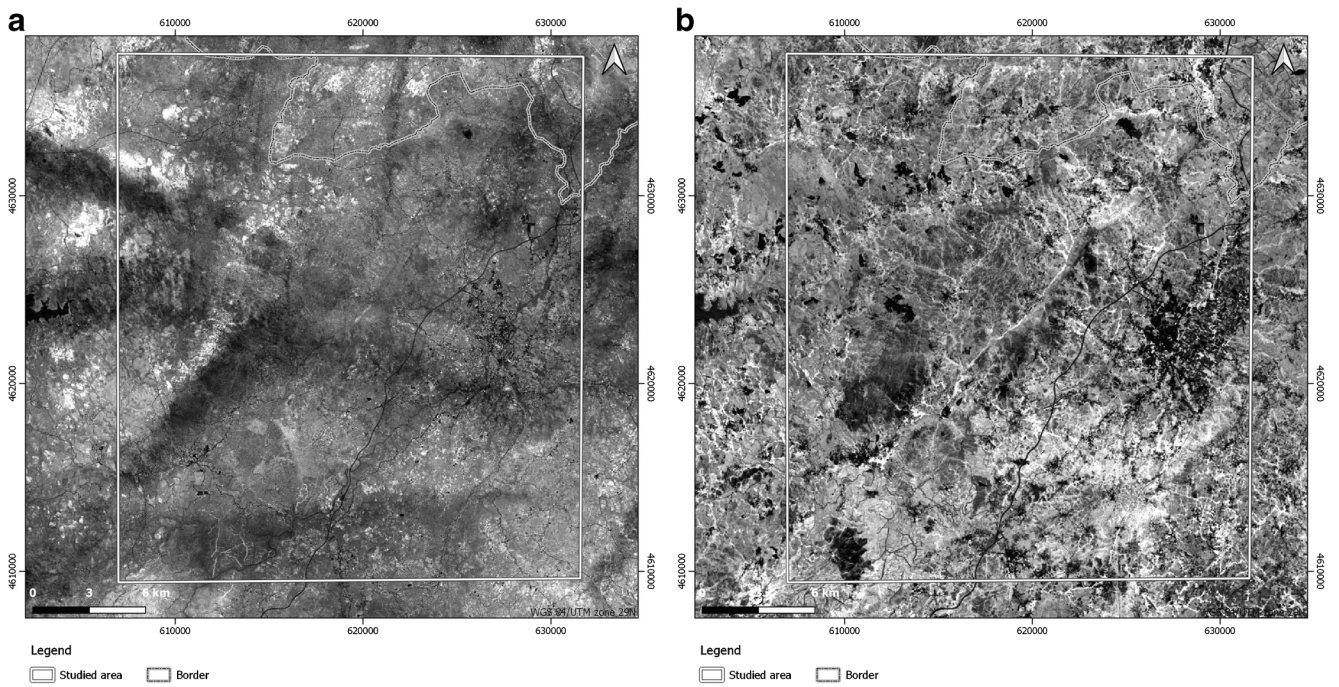


Fig. 4 Highlighted altered minerals through band rationing. **a** 4/2 ratio image mapping iron oxides in bright pixels. **b** 6/7 ratio image mapping hydroxyl-bearing minerals in bright pixels

Another composite band ratio tested was the Kaufmann ratio (7/5, 5/4, 6/7) (Fig. 5b). In this composite image, iron oxides are purple to pink; ferrous minerals, rock exposure, and urban structures are in red; and vegetation is shown in light blue to blue.

Principal component analysis

PCA was carried out using SCP (Congedo 2016) on Landsat 8 imagery with no atmospheric or radiometric correction, as it is not required. The eigenvector matrix used to calculate PCA

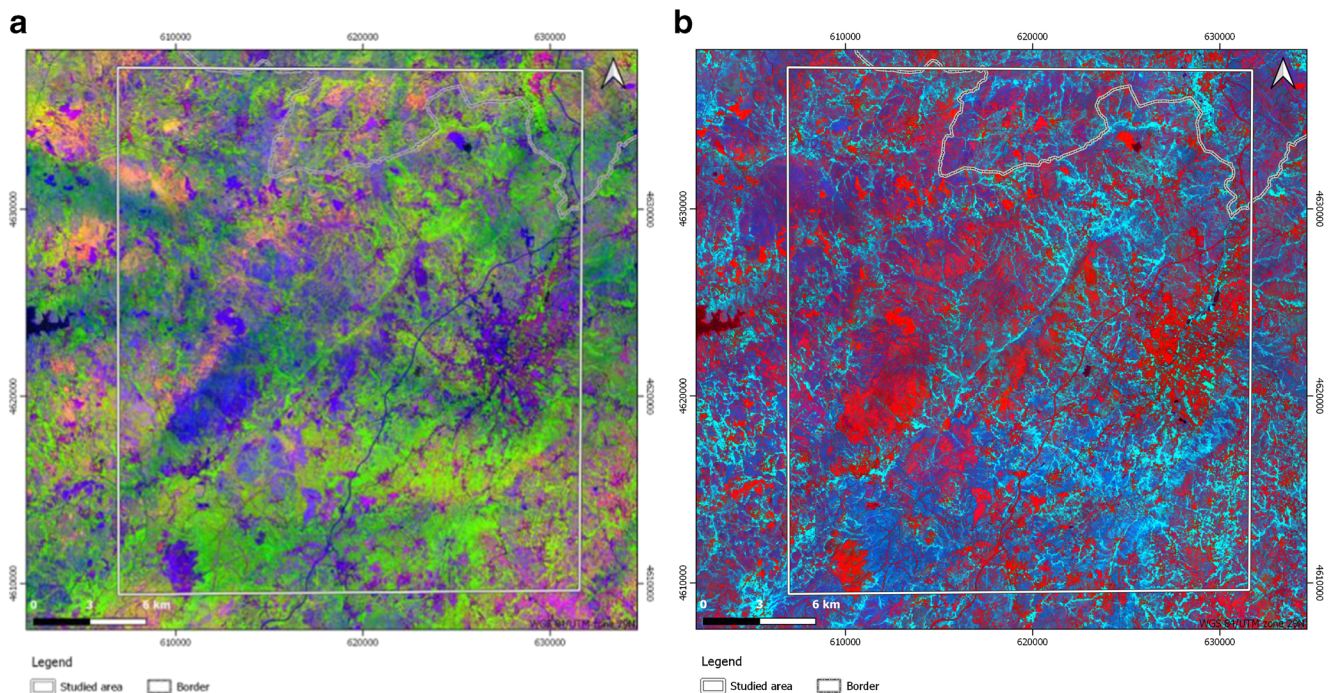


Fig. 5 RGB composite images using band ratios to discriminate hydrothermally altered areas. **a** Sabin's ratio (RGB 4/2, 6/7, 6/5). **b** Kaufmann ratio (RGB 7/5, 5/4, 6/7)

was analyzed to identify which PC more accurately highlights hydrothermally altered zones. This technique was applied in a standard method, where all six bands were analyzed, and a selective method, using sets of four selected bands, based on the position of spectral signatures of alteration minerals.

Standard method

A standard PCA was applied using six Landsat 8 bands (2, 3, 4, 5, 6, and 7) outputting an eigenvector matrix, listed in Table 2. The result allowed us to identify the PC that had more useful spectral information than that from Landsat 8 bands, in contrast to the original bands.

Table 2 lists image statistics, eigenvalues, and eigenvector loadings for PC analysis using the six bands. Each PC contains six eigenvector loadings corresponding to linear combinations of weighted input band images. The first principal component (PC1), indicated by the accounted variance, contains 94.5% of the total data variance. This PC is responsible for the overall scene brightness or albedo. Based on the magnitude analysis and signs of eigenvector loadings (positive or negative), the PC containing hydrothermal alteration minerals and vegetation spectral properties was identified. PC2 contains 3.9% of the data variance and the eigenvector loadings are dominated by vegetation due the high loading in band 5 (mapped in dark pixels because of the negative sign), representing the difference between visible and NIR bands. The eigenvector loadings for PC3, with 1.4% of variance, represent the contrast of SWIR bands between visible and NIR bands. The remaining three PCs contain information highlighting hydrothermal alteration related to the spectral response to iron oxides (absorption in band 2 and higher reflectance in band 4) and hydroxyl-bearing minerals (absorption in band 7 and higher reflectance in band 6). To highlight iron oxide-rich areas, PCs with moderate to large eigenvector loadings for bands 2 and 4, with opposite signs, are selected. Iron oxide minerals are mapped in PC4 as bright pixels (band

2 is negative and band 4 is positive) and in PC5 as dark pixels (band 2 is positive and band 4 is negative). Hydroxyl-bearing minerals are highlighted as dark pixels in PC4 and PC5, because in both the contribution of band 6 is negative and that of band 7 is positive. In PC6, hematite is mapped as dark pixels because the contribution is negative from band 4 and positive from band 3.

Based on the PCA outputs (Table 2), an RGB combination was computed in order to identify hydrothermally altered rocks, combining PC4, PC5, and PC6. For this image, PC5 was negated and stretched to highlight hydroxyl-bearing minerals and iron oxides in bright pixels. The same was done for PC6.

The output image (Fig. 6) discriminates different features better than the previously considered methods. Urban areas are shown in pink, iron oxide-rich zones in yellow and pink, clay-rich areas in light blue, and vegetation in brownish tones. This RGB combination also shows good lithological contrast at regional scale.

Selective PCA method

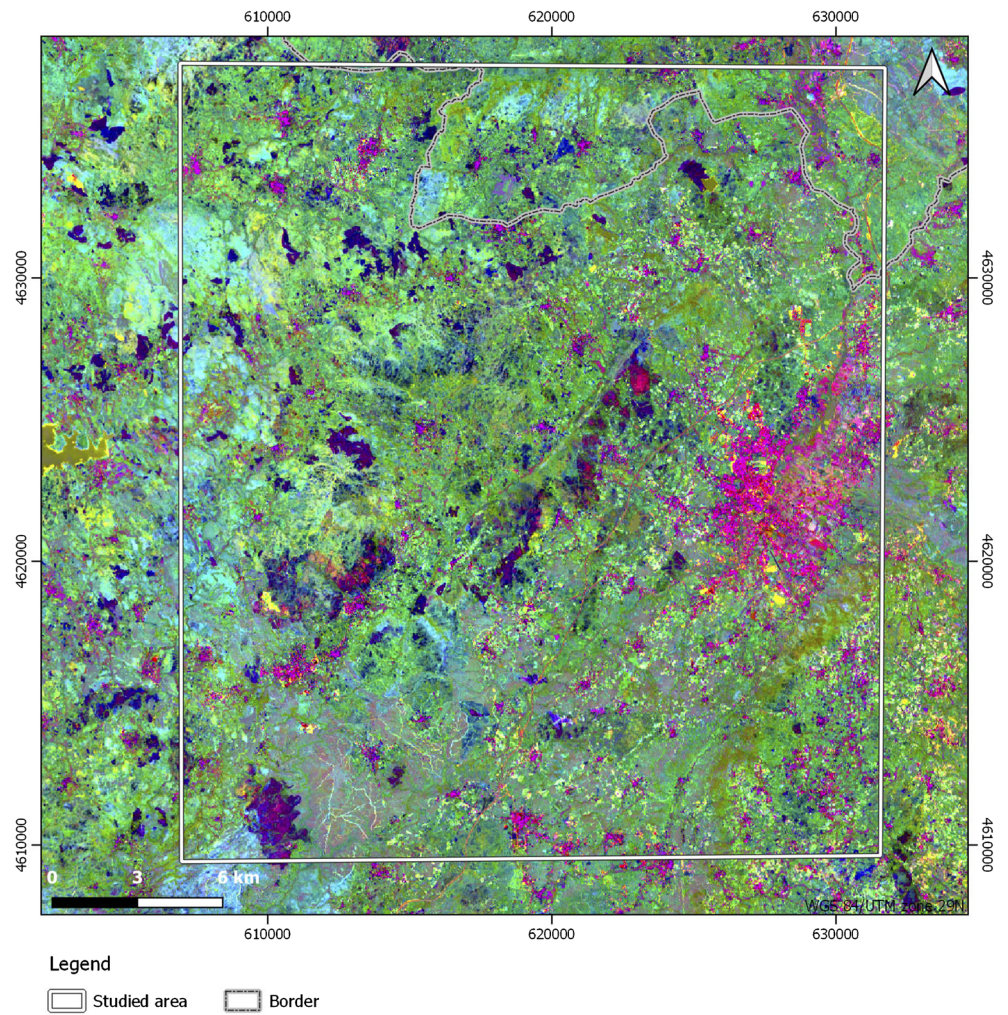
Following the Crósta technique proposed by Loughlin (1991), selective PCA was performed to increase the highlight definition of a mineral class. The band subsets were selected based on the position of spectral signatures of alteration minerals, as hydroxyl-bearing minerals and iron oxides, in the VNIR and SWIR bands.

To map hydroxyl-bearing minerals, a subset including bands 2, 4, 5 and 6 were selected and analyzed (Table 3). A similar interpretation to the standard PCA was made for the eigenvalue loading matrix. PC1 corresponds to albedo with 94.8% of data variance; PC2 highlights dense vegetated areas as bright pixels, with data variance of 3.6%; PC3 describes the contrast between visible/NIR and SWIR bands, representing 1.5% of data variance; and PC4 highlights hydroxyl-bearing minerals as dark pixels, with a data variance of 0.04%. The

Table 2 Eigenvector loadings from PCA Landsat 8 bands 2–7

	PC1	PC2	PC3	PC4	PC5	PC6
Band 2	-0.3354	0.4410	0.4777	-0.5367	0.1800	-0.3799
Band 3	-0.3224	0.3185	0.2795	0.0821	-0.1176	0.8342
Band 4	-0.3059	0.3495	0.0576	0.6690	-0.4202	-0.3960
Band 5	-0.6005	-0.7303	0.2953	0.1004	0.0781	-0.0511
Band 6	-0.4583	0.0110	-0.6390	-0.4307	-0.4426	0.0128
Band 7	-0.3454	0.2200	-0.4414	0.2490	0.7584	0.0128
Eigenvalues	167,154,331.62	6,971,372.53	2,553,863.80	97,033.74	40,158.80	8988.42
Accounted variance	94.53	3.94	1.44	0.055	0.02	0.0051
Cumulative variance	94.53	98.47	99.92	99.97	99.99	100

Fig. 6 RGB combination image using principal components as input bands (PC4, PC5, PC6). Different features are better discriminated with urban areas represented in pink, iron oxide-rich zones in yellow and pink, and clay-rich areas in light blue



PC4 image is negated to highlight hydroxyl-bearing minerals in bright pixels, and it was used as a hydroxyl image (H) (Fig. 7a) in the final RGB combination. This image has a negative contribution from vegetation in the NIR band (band 5), which has a similar response to hydroxyls in the SWIR bands.

Table 4 presents the loading results from PCA of bands 2, 4, 5, and 6 for iron oxide mineral enhancement. PC1 corresponds to the albedo image with 94.5% of variance data; PC2, with 4.1% of variance, represents the vegetated areas as darker

pixels; PC3 represents the contrast of SWIR band between visible and NIR bands; and PC4 indicates high positive and high negative eigenvector loading for band 2 (0.8136) and band 4 (-0.5099), respectively, so in this image, pixels with an abundance of iron oxide minerals are bright (Fig. 7b). This PC4 image is our iron oxide image (F).

The greyscale hydroxyl and iron oxide images from selective PCA shown in Fig. 7 are useful to locate anomalous concentrations of each mineral subset, highlighted by bright

Table 3 Eigenvector loading for principal component analysis of Landsat 8 bands 2, 5, 6, and 7 to map hydroxyl-bearing minerals

	PC1	PC2	PC3	PC4
Band 2	-0.3666	-0.5343	0.7424	-0.1701
Band 5	-0.6766	0.7000	0.1964	0.1166
Band 6	-0.5113	-0.2357	-0.5612	-0.6067
Band 7	-0.3826	-0.4110	-0.3089	0.7677
Eigenvalues	134,583,947.66	5,151,351.73	2,195,471.34	57,628.11
Accounted variance	94.79	3.63	1.55	0.041
Cumulative variance	94.79	98.41	99.96	100

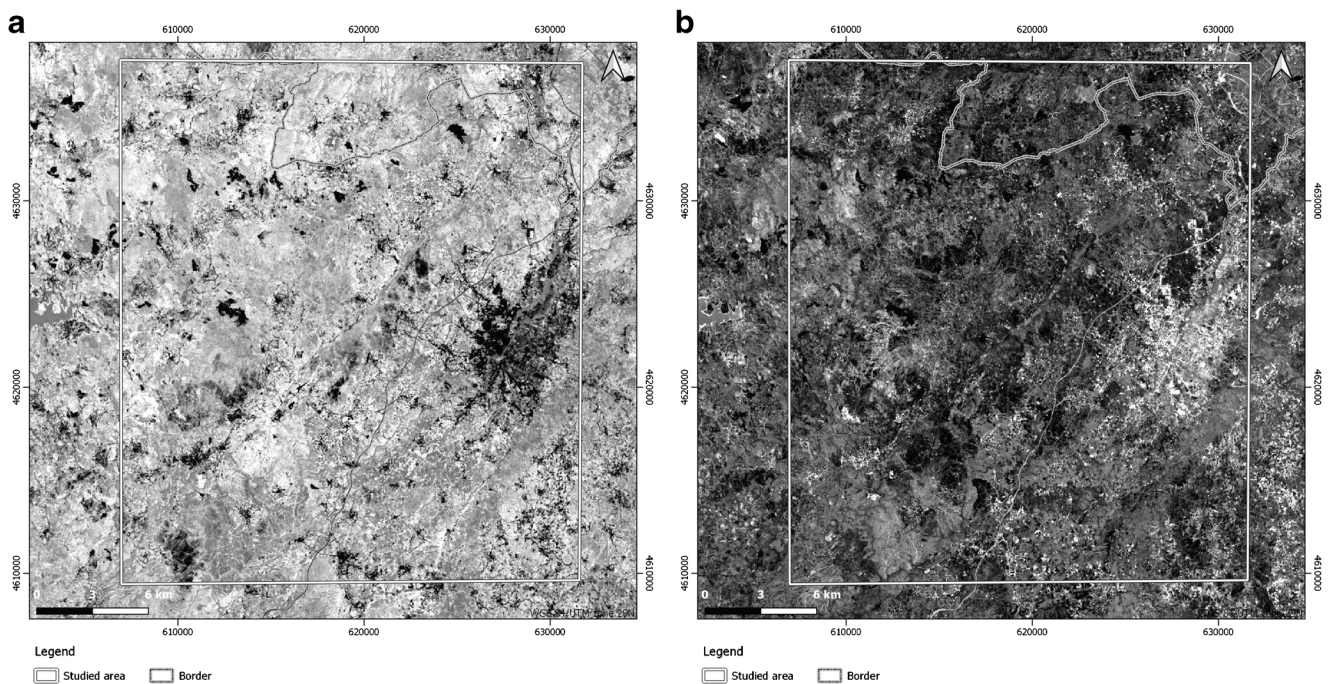


Fig. 7 Principal component images resulting from selective PCA. **a** Hydroxyl (H). **b** Iron oxide (F). Each mineral subset is highlighted by bright pixels

pixels. The combination of these images produced an image highlighting anomalous concentrations of both iron oxides and hydroxyl minerals (H+F).

A Crósta composite image was created combining the H, H+F, and F images, with the bright pixels favorably enhanced (Fig. 8). In this image, argilized and iron-stained alteration zones are white to pale light blue, considered more favorable for mineral occurrence (most prospective areas). Areas that are more iron stained than argilized are shown in blue and light blue. In contrast, zones that are more argilized than iron stained are imaged in bright reddish to orange. Intense dark or deep blue pixels in association with the alteration colors can represent an alteration type associated with intensely argilized or silicified and heavily iron-stained rocks, which pixels in these areas have higher reflectance in band 7 than band 6 (Loughlin 1991). This alteration can be recognized in hydroxyl images by very dark pixels closely associated with bright

pixels, representing hydroxyl-altered areas. However, not all intense dark blue to black areas correspond to hydrothermally altered rocks. Burned vegetation can have a similar spectral response, and SWIR bands are also sensitive to variations in vegetation. Therefore, it is important to recognize alterations around these dark areas.

Structural feature extraction

Structural lineament extraction was carried out via visual interpretation of false color composites described above and using Shuttle Radar Topography Mission (SRTM) digital elevation models (DEMs). Lineaments are identified by physiographic characteristics detected due to the abrupt discontinuity in image brightness and tonal change in the satellite data, excluding man-made lineaments, vegetation alignments, and other surface features (Fig. 9). Interpreted structural lineaments mainly strike NNE-SSW, ENE-WSW, and NNW-SSE in this region.

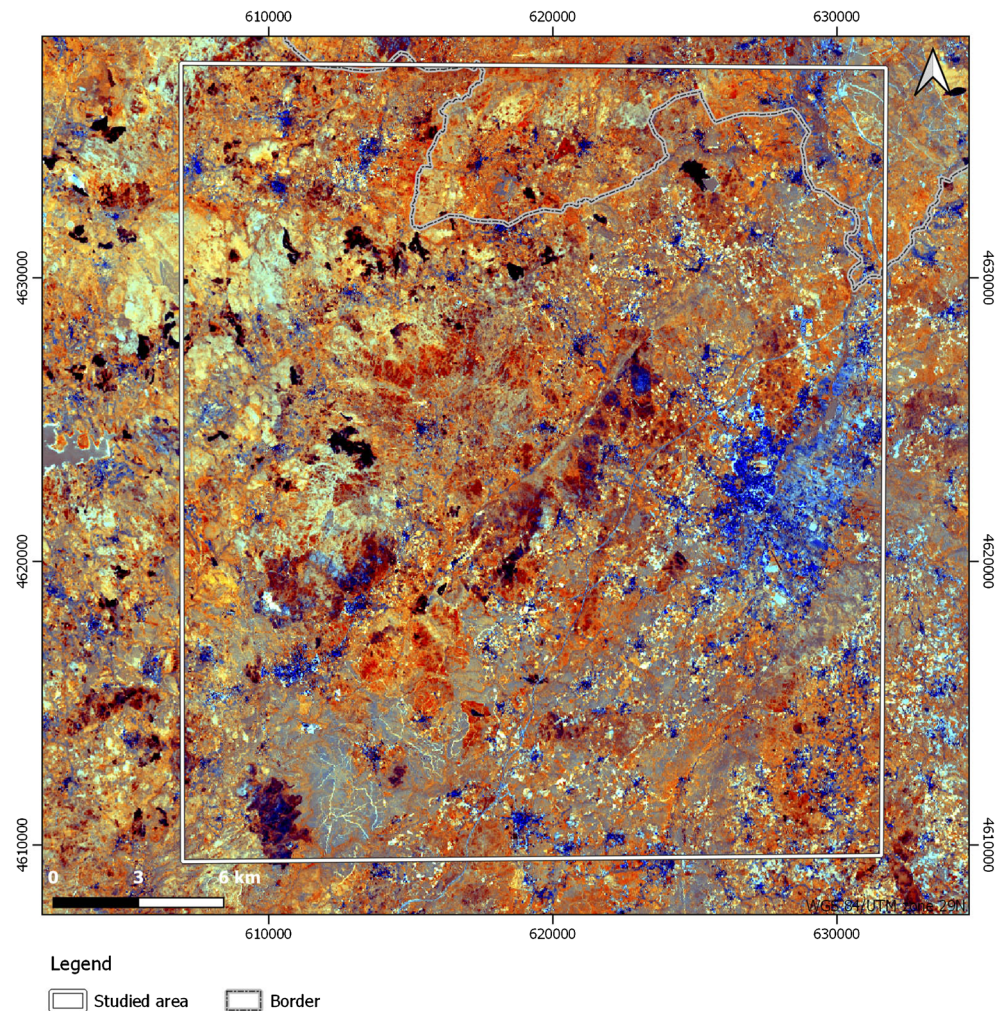
Table 4 Eigenvector loading for principal component analysis of Landsat 8 bands 2, 4, 5, and 6 to map iron oxide minerals

	PC1	PC2	PC3	PC4
Band 2	-0.3753	0.5876	0.5039	-0.5099
Band 4	-0.3423	0.4694	0.0209	0.8136
Band 5	-0.6884	-0.6473	0.3186	0.0757
Band 6	-0.5178	0.1242	-0.8026	-0.2689
Eigenvalues	130,153,939.4	5,633,888	1,851,818	90,046.69
Accounted variance	94.50	4.10	1.34	0.065
Cumulative variance	94.50	98.60	99.93	100

Validation with historical data and field observations

The available historical exploration data was accessed to validate the results of remote sensing image processing. Data from geochemical soil sampling carried out by COGEMA in 1990 were used (COGEMA 1990). The soil sampling campaign focused on Limarinho deposit, partially covering the eastern flank of Leiranco mountain. We used this data because Limarinho is a well-studied deposit with known gold occurrence. As gold mineralization is highly correlated with arsenopyrite, we used

Fig. 8 RGB combination using H, H+F, and F images, the Crósta composite image. Alteration zones both argilized and iron stained are represented in white pale to light blue, areas rich in iron oxides in blue to light blue, and areas more argilized in bright reddish to orange. Some dark blue pixels can represent areas intensely argilized or silicified, and heavily iron-stained rocks



the arsenic soil anomaly distribution plot to analyze and identify potential anomalous areas (Fig. 10) (Noronha et al. 2000; Cepedal et al. 2013; Lima et al. 2014a; Fuertes-Fuente et al. 2016).

Remote sensing analysis did not identify the Limarinho area because of the dense vegetation, and mainly the soil remobilization caused by extensive Roman mining, as demonstrated by abundant tailings, and more recent agricultural activities (Lima et al. 2011; Lima et al. 2014a). By the analysis of Fig. 10, a correlation with the results of remote sensing and historical geochemical soil samples is observed. The arsenic anomaly on the flank of Leiranco mountain matches with the hydrothermally altered area highlighted by remote sensing, and we assume that this soil anomaly continues through the top of the mountain. In addition, interpreted structures reveal spatial correlation with these arsenic soil anomalies.

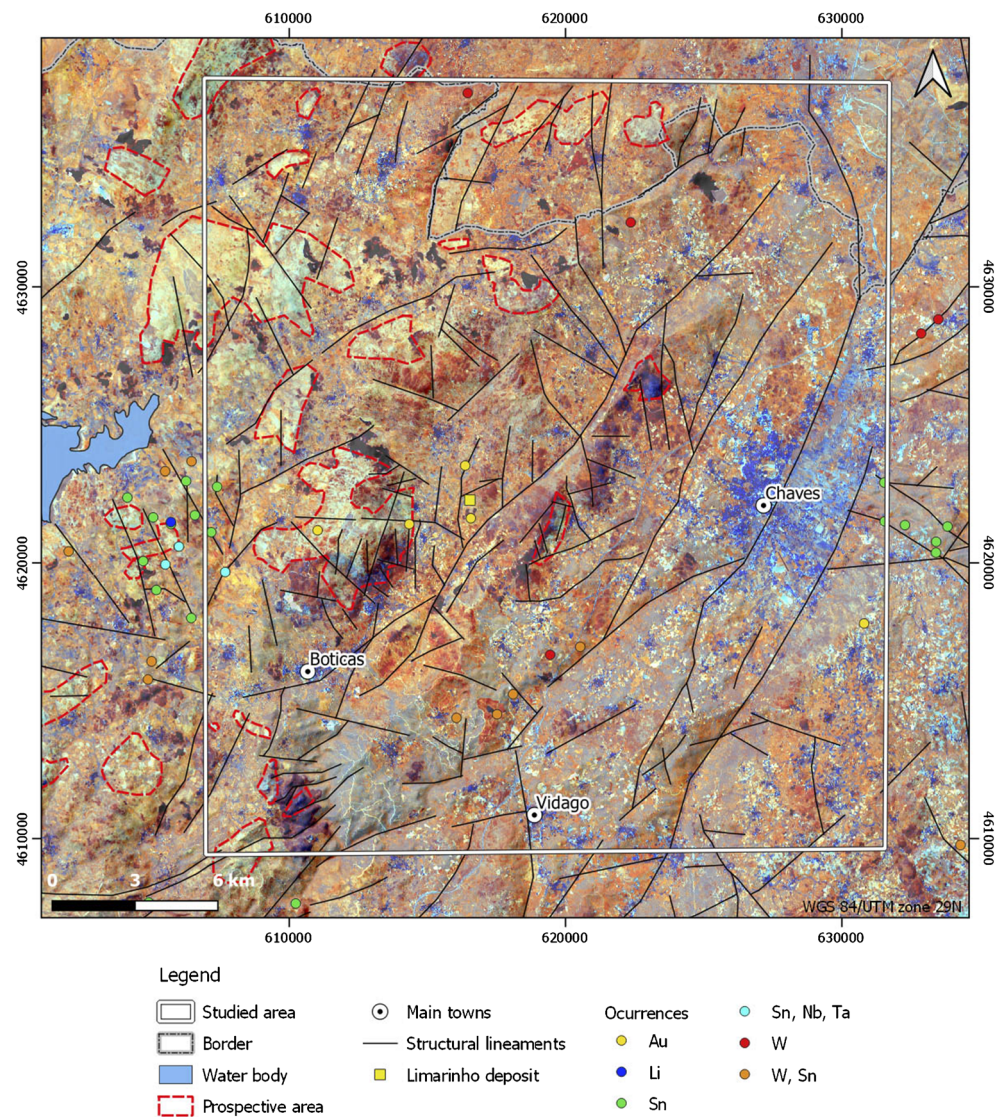
Leiranco mountain was identified as a potential area for mineral occurrence due to the strong hydrothermal alteration highlighted in the satellite imagery analysis (Fig. 10). Similarly, to Limarinho, in this area, there is a high density of quartz veins rich in arsenopyrite, along with associated

alteration zones such as argillic, argillic silica, and iron oxide alteration. Outcrop views of these veins and associated alteration are shown in Fig. 11. The remote sensing analysis and field observations (Figs. 10 and 11) indicated that hydrothermal alterations around Leiranco mountain are widely extended. Granite outcrops are hydrothermally altered, with iron oxides and hydroxyl-bearing minerals. The alteration is often associated with thin parallel quartz arsenopyrite-bearing veins, and gold mineralization is typically related to these alteration zones associated with arsenopyrite (Noronha et al. 2000; Cepedal et al. 2013; Lima et al. 2014a; Fuertes-Fuente et al. 2016).

Discussion

In geological exploration, target generation is an important stage involving high risk and defining prospective areas requires geological information, which is sometimes unavailable or inaccurate. Furthermore, field reconnaissance is time-consuming and can be difficult and expensive. Remote sensing has been

Fig. 9 Interpreted structural lineaments over the Crósta composite image. Most prospective areas are outlined in dashed red lines



successfully applied to map hydrothermal alteration zones associated with mineralization in different parts of the world (Sabins 1999; Robert et al. 2007; Cudahy 2016; Pour et al. 2018b; Bolouki et al. 2020; Booyesen et al. 2019; Eldosouky et al. 2020; Pour et al. 2019; Beygi et al. 2020; Sekandari et al. 2020; Takodjou Wambo et al. 2020; Traore et al. 2020). Remote sensing data along with other gathered geological data, such as geochemical and geophysical information, can be integrated to produce a potential mineral occurrence map (Rajesh 2004; Porwal and Kreuzer 2010; Pour and Hashim 2015; Manuel et al. 2017; Xiang et al. 2020). In this investigation, different satellite imagery processing methods were applied to Landsat 8 data to map hydroxyl-bearing and iron oxide minerals, and to extract structural lineaments, defining prospective targets in Boticas-Chaves region. Hydrothermal alteration minerals were mapped based on the spectral absorption characteristics for iron oxides and hydroxyl-bearing minerals by implementing RGB combinations, band ratios, and PCA

algorithms to the spectral bands of Landsat 8. RGB combinations, such as 573 and 567, were capable of distinguishing different features and enhancing alteration on rock outcrops. However, this imagery analysis method has strong influence of noise and it is difficult to separate signals from different mineral compositions, which makes this type of analysis the most challenging to interpret. For this method, best results can be obtained in remote areas without signal noise from urban areas and in less vegetated regions.

Band ratios were applied to eliminate topographic effects and reduce noise, enhancing the spectral characteristics. The band ratio combination of 4/2 was applied to highlight iron oxides and the band ratio 6/5 was generated in order to map ferrous minerals. Both band ratios contributed to the lithological interpretation on a regional scale. Granites showed a good correlation with the highlighted areas, mostly because of the alteration of biotite. To map hydroxyl-bearing minerals, the band ratio 6/7 was used.

Fig. 10 Arsenic anomaly from historical soil sampling campaign plotted with interpreted structural lineaments and most prospective areas outlined in dashed red lines

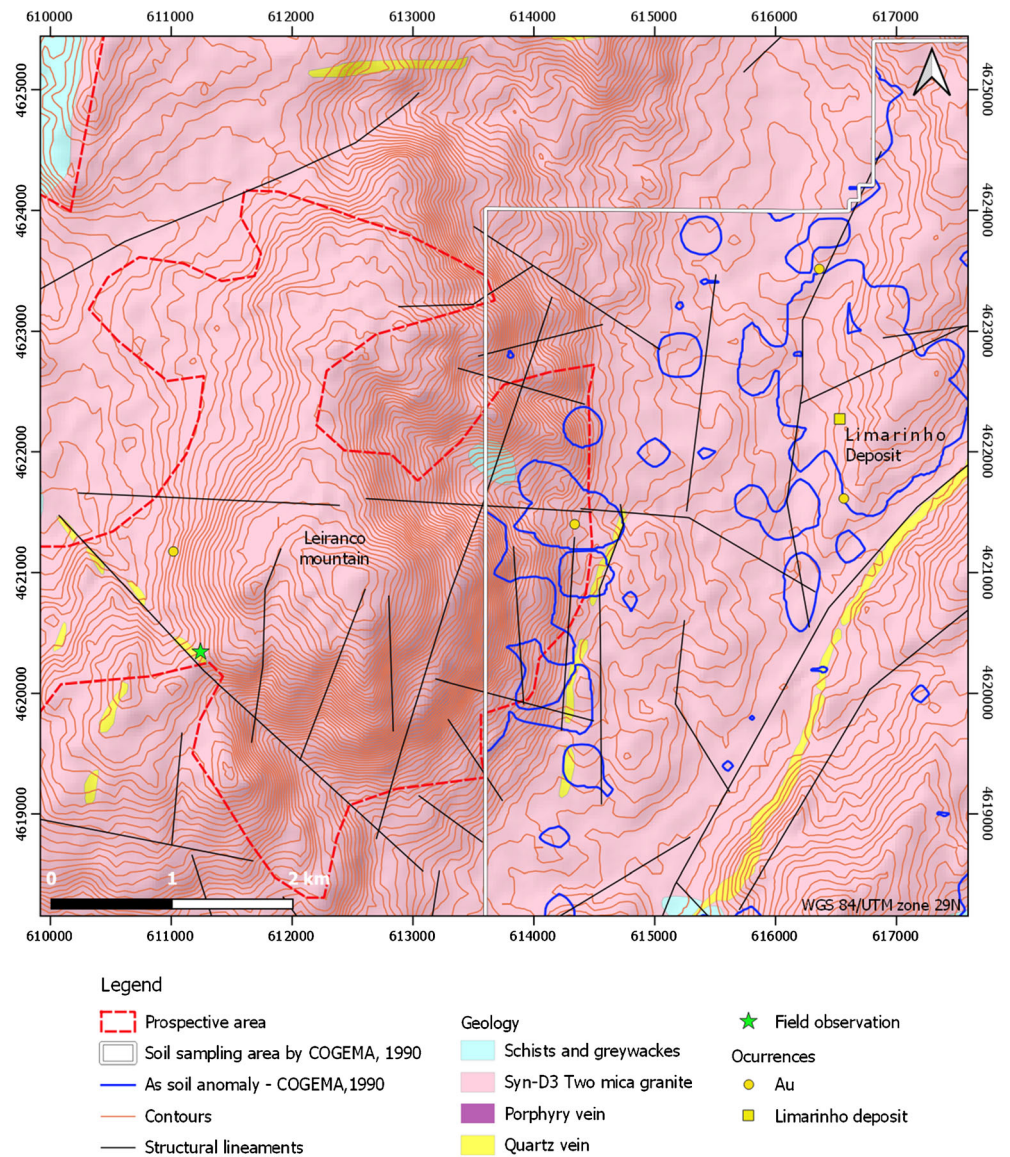
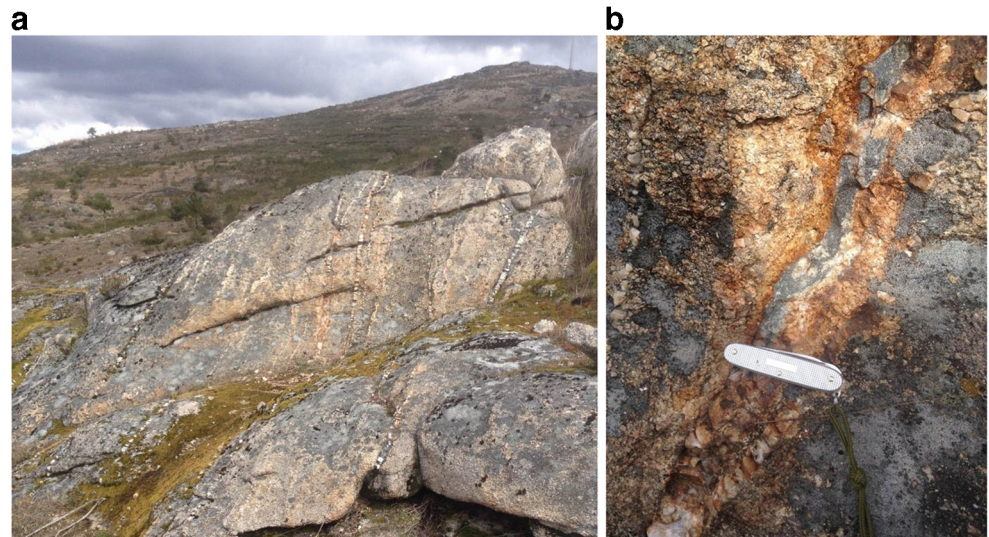


Fig. 11 Field photographs of high-density parallel quartz veins and typical associated hydrothermal alteration on Leiranco mountain. **a** View of parallel N40°; subvertical quartz arsenopyrite-bearing veins hosted by two-mica granite. **b** Oxidized and argillized granite in the selvages of quartz arsenopyrite-bearing veins



The results show clay minerals concentrated along water lines that can be associated with structural elements as faults. However, SWIR bands are sensitive to moisture in vegetation and soil and can also highlight certain types of vegetation (Murakami 2006; USGS 2012; Ferreira et al. 2015; Cudahy 2016; Ridwan et al. 2018). Ploughed fields are also enhanced by this band ratio, possibly due to soil remobilization exposing higher concentrations of these minerals at the surface. The band ratio method not only proved to be a better technique in comparison with single band RGB combinations, highlighting more features, but also demonstrated some limitations in mapping hydrothermally altered rocks.

PCA methods proved to be the most effective and reliable in the identification of iron oxides and hydroxyl-bearing minerals. Standard and selective PCA outputs demonstrated the capability to efficiently discriminate different features and highlight potentially hydrothermally altered areas. Selective PCA is even more effective, as it can separate hydroxyl-bearing minerals and iron oxides, in defining unique PCs for specific mineral subsets. The combination of selective PCA outputs in an RGB image produces a better quality image, enhancing the identification of alteration types and intensities.

Lineaments were extracted by relying on visual interpretation of remote sensing imagery and the SRTM elevation model. Geological lineaments such as faults and joints are of interest because they can serve as conduits for mineralizing fluids. Textural characteristics of structural features are recognizable by multispectral imagery analysis, allowing to identify lineaments. It is important to mention that some of the mapped features may not be of geologic nature, but good correlation is verified between the published geological maps (Fig. 1) and the visually interpreted lineaments (Fig. 9).

Subsequently, potential prospective areas for the study zone were defined (Fig. 9). Hydrothermally altered rocks located adjacent to the NNE-SSW, NNW-SSE, and ENE-WSW structures, which likely worked as mineralizing fluid conduits, were identified as high potential for gold mineralization occurrence. Known mineral occurrences reveal a spatial relationship with the structural features in the study area, and the historical geochemistry data and field observations in the Leiranco mountain present a strong correlation with the remote sensing analysis. However, some known occurrences in the study area, such as the Limarinho deposit, do not reveal a strong signature of hydrothermal alteration minerals, which can be explained by spatial resolution and vegetation cover, and mainly soil remobilization caused by extensive Roman mining (Lima et al. 2011; Lima et al. 2014a). More advanced analysis should be carried out to define more precisely the areas of interest, mask all noise sources, such as urban areas and vegetation, and compare the results with other satellite imagery. Computational algorithms can also be employed to optimize lineament extraction. Nevertheless, applied analyses to Landsat 8 satellite imagery were capable to map iron oxides and hydroxyl-bearing

minerals, and allowed the identification of important structure lineaments, indicating highly prospective targets.

Conclusion

This investigation aimed to demonstrate the applicability of Landsat 8 imagery analysis to an area situated in a mild and humid climatic zone and to prove that it is a suitable complement to early-stage fieldwork. Remote sensing methodologies, such as RGB combination, band ratio, and PCA methods were applied to obtain relevant geological features to outline areas with potential for gold mineralization occurrence in Boticas-Chaves region, Portugal. The application of selective PCA proved to be the most efficient to map pixels containing the spectral signature for specific alteration minerals. The occurrence of both hydrothermal alteration minerals, hydroxyl and iron oxide, spatially close to NNE-SSW, ENE-WSW and NNW-SSE structural features trends, are considered highly prospective zones for gold mineralization in the study area (Fig. 9) and can be used as a target for exploration works. The results of this study demonstrate that the applied remote sensing methods provide valuable geological information that can be used as an efficient evidential layer for mineral prospectivity mapping and it is a cost-efficient and time-saving tool for mineral exploration, which applied in other regions can efficiently identify new potentially mineralized areas.

Funding The authors received financial support provided by FCT—Fundação para a Ciência e a Tecnologia, where Rui Frutuoso is financially supported within the compass of the ERA-MIN/0005/2018—AUREOLE project, FEDER through operation POCI-01-0145-FEDER-007690 funded by the Programa Operacional Competitividade Internacionalização—COMPETE2020 and by National Funds through FCT within the ICT (reference UIDB/04683/2020).

Declarations

Conflict of interest The authors declare no competing interests.

References

- Ali A, Pour A (2014) Lithological mapping and hydrothermal alteration using Landsat 8 data: a case study in Ariab mining district, red sea hills, Sudan. *Int J Sci* 3(3):199–208. <https://doi.org/10.14419/ijbas.v3i3.2821>
- Beygi S, Talovina IV, Tadayon M, Pour AB (2020) Alteration and structural features mapping in Kacho-Mesqal zone, Central Iran using ASTER remote sensing data for porphyry copper exploration. *Int J Image Data Fusion*:1–21. <https://doi.org/10.1080/19479832.2020.1838628>
- Bolouki SM, Ramazi HR, Maghsoudi A, Pour AB, Sohrabi G (2020) A remote sensing-based application of Bayesian networks for epithermal gold potential mapping in Ahar-Arasbaran area, NW Iran. *Remote Sens* 12:105. <https://doi.org/10.3390/rs12010105>

- Booyens R, Gloaguen R, Lorenz S, Zimmermann R, Andreani L, Ne PAM (2019) The potential of multi-sensor remote sensing mineral exploration: examples from Southern Africa. Proceedings of the IGARSS 2019 – IEEE International Geoscience and Remote Sensing Symposium, edited by IEEE, 6027–6030. Yokohama, Japan. <https://doi.org/10.1109/IGARSS.2019.8899081>
- Cabral J. (1995) Neotectónica em Portugal continental, Memórias 31. Instituto Geológico e Mineiro. 265p.
- Cardoso-Fernandes J, Lima A, Teodoro A (2018) Sentinel-2 data as a tool for structural mapping. Conference: VIII Congresso Jovens Investigadores em Geociências, LEG. Estremoz.
- Cardoso-Fernandes J, Teodoro AC, Lima A (2019) Remote sensing data in lithium (Li) exploration: a new approach for the detection of Li-bearing pegmatites. *Int J Appl Earth Obs Geoinf* 76:10–25. <https://doi.org/10.1016/j.jag.2018.11.001>
- Cardoso-Fernandes J, Teodoro AC, Lima A, Perrota M, Roda-Robles E (2020a) Detecting Lithium (Li) mineralizations from space: current research and future perspectives. *Appl Sci (Switzerland)* 10(5): 1785. <https://doi.org/10.3390/app10051785>
- Cardoso-Fernandes J, Teodoro AC, Lima A, Roda-Robles E (2020b) Semi-automatization of support vector machines to map lithium (Li) bearing pegmatites. *Remote Sens* 12(14):2319. <https://doi.org/10.3390/rs12142319>
- Catalán JR., Arenas R, García F, Cuadra P, Gómez Barreiro J, Abat, J, Castiñeiras P, Fernández-Suárez J, Martínez S, Andonaegui P, et al (2007) Space and time in the tectonic evolution of the northwestern Iberian Massif: implications for the Variscan belt. Vol. 200. ISBN 978-0-8137-1200-0.
- Cepedal A, Martínez-Abad I, Fuertes-Fuente M, Lima A (2013) The presence of plumbago ingodite and a rare Bi-Pb tellurosulfide, Pb₃Bi₄Te₄S₅, in the Limarinho gold deposit, northern Portugal. *Can Mineral* 51:643–651. <https://doi.org/10.3749/canmin.51.4.643>
- COGEMA (1990) Sector de Poço das Freitas. Relatório de trabalhos. Unpublished report: 49 p.
- Congedo L (2016) Semi-automatic classification plugin documentation. Release 6.0.1.1. <https://doi.org/10.13140/RG.2.2.29474.02242/1>
- Crósta A, Moore JM (1989) Enhancement of Landsat Thematic Mapper imagery for residual soil mapping in SW Minas Gerais State, Brazil: a prospecting case history in Greenstone belt terrain. Proceedings of the 7th (ERIM) Thematic Conference: Remote Sensing for Exploration Geology. 1173–1187.
- Crósta A, Rabelo A (1993) Assessing Landsat/TM for hydrothermal alteration mapping in central-western Brazil. Proceedings of the Ninth Thematic Conference on Geologic Remote Sensing: Exploration, Environment, and Engineering, Vols 1 and 2: 1053–1061
- Crósta A, Souza Filho C, Azevedo F, Brodie C (2003) Targeting key alteration minerals in epithermal deposits in Patagonia, Argentina, using ASTER imagery and principal component analysis. *Int J Remote Sens* 24:4233–4240. <https://doi.org/10.1080/0143116031000152291>
- Cudahy T (2016) Mineral mapping for exploration: an Australian journey of evolving spectral sensing technologies and industry collaboration. *Geosciences* 6:52. <https://doi.org/10.3390/geosciences6040052>
- Dias G, Leterrier J, Mendes A, Simões PP, Bertrand JM (1998) U-Pb zircon and monazite geochronology of post-collisional Hercynian granitoids from the Central Iberian Zone (Northern Portugal). *Lithos* 45:349–369. [https://doi.org/10.1016/S0024-4937\(98\)00039-5](https://doi.org/10.1016/S0024-4937(98)00039-5)
- Drury SA (2001) Image interpretation. In *Geology*, edited by Nelson Thornes. Blackwell Science, USA. ISBN 978-0-632-05408-4.
- Eldosouky AM, Sehsah H, Elkhatieb SO, Pour AB (2020) Integrating aeromagnetic data and Landsat-8 imagery for detection of post-accretionary shear zones controlling hydrothermal alterations: The Allaqi-Heiani Suture zone, South Eastern Desert, Egypt. *Adv Space Res* 65(3):1008–1024. <https://doi.org/10.1016/j.asr.2019.10.030>
- Farias P, Gallastegui G, González Lodeiro L, Marquín J, Martín Parra LM, Martínez Catalán JR, Pablo Maciá JG, Rodríguez Fernández LR (1987) Aportaciones al conocimiento de la litoestratigrafía y estructura de Galicia Central. *Memórias da Faculdade de Ciências da Universidade do Porto* 1:411–431
- Ferreira N, Iglesias M, Noronha F, Pereira E, Ribeiro A, Ribeiro ML (1987) Granitoides da Zona Centro Ibérica e seu enquadramento geodinâmico in *Geologia de los Granitoides y Rocas asociadas del Macizo Hesperico*. Bea, edited by: F. C., Camicero, A., Gonzalo, J. C., López Plaza, M., Rodríguez Alonso, M.D., Rueda, Madrid. 37–51.
- Ferreira MP, Zortea M, Zanotta DC, Féret JB, Shimabukuro YE, Souza Filho CR (2015) On the use of shortwave infrared for tree species discrimination in tropical semideciduous forest. *Int Arch Photogramm Remote Sens Spat Inf Sci XL-3/W3:473–476*. <https://doi.org/10.5194/isprsarchives-XL-3-W3-473-2015>
- Fuertes-Fuente M, Cepedal A, Lima A, Dória A, Ribeiro M, Guedes A (2016) The Au-bearing vein system of the Limarinho Deposit (Northern Portugal): genetic constraints from Bi-chalcogenides and Bi-Pb-Ag sulfosalts, fluid inclusions and stable isotopes. *Ore Geol Rev* 72:213–231. <https://doi.org/10.1016/j.oregeorev.2015.07.009>
- Gabr S, Ghulam A, Kusky T (2010) Detecting areas of high-potential gold mineralization using ASTER data. *Ore Geol Rev* 38:59–69. <https://doi.org/10.1016/j.oregeorev.2010.05.007>
- Goetz AF, Rowan LC, Kingston MJ (1982) Mineral identification from orbit: initial results from the shuttle multispectral infrared radiometer. *Science* 218:1020–1024. <https://doi.org/10.1126/science.218.4576.1020>
- Goetz A (2009) Three decades of hyperspectral remote sensing of the Earth: a personal view. *Remote Sens Environ* 113:S5–S16. <https://doi.org/10.1016/j.rse.2007.12.014>
- Hunt GR (1977) Spectral signatures of particulate minerals in the visible and near infrared. *Geophysics* 42:501–513. <https://doi.org/10.1190/1.1440721>
- Jain N, Singh R, Roy P, Martha TR, Vinod Kumar K, Chauhan P (2018) Mapping of hydrothermally altered zones in Aravalli Supergroup of rocks around Dungarpur and Udaipur, India, using Landsat-8 OLI and spectroscopy. *Arab J Geosci* 11:455. <https://doi.org/10.1007/s12517-018-3799-5>
- Julivert M, Fontboté JM, Ribeiro A, Conde LEN (1974) Mapa Tectónico de la Península Ibérica y Baleares, Scale 1:1000.000. *Memória Explicativa*. Instituto Geológico y Minero de España, Madrid.
- Nikolakopoulos KG, Tsombos PI, Skianis GA, Vaiopoulos DA (2008) EO-1 Hyperion and ALI bands simulation to Landsat 7 ETM+ bands for mineral mapping in Milos Island. *Proc. SPIE 7110, Remote Sensing for Environmental Monitoring, GIS Applications, and Geology VIII*, 711010. <https://doi.org/10.1117/12.798745>
- Lima A, Matias Rodríguez R, Fonte J, Pires H (2014a) The historic gold mining in the high Terva river basin (Northern Portugal). *Comunicações Geológicas III* 101:1289–1293 <https://repositorio-aberto.up.pt/handle/10216/82428>
- Lima A, Matias R, Mendonça A (2011) Contribuição para o estudo da Mineração Romana de ouro na Bacia do Rio Terva. In *Povoamento e exploração dos recursos mineiros na Europa Atlântica Ocidental*, edited by: Martins, C.M.B., Bettencourt, A.M.S., Martins, J.I.F.P., Carvalho, J., 241–256. Centro de Investigação Transdisciplinar “Cultura, Espaço e Memória”/Associação Portuguesa para o Estudo do Quaternário (CITCEM/APEQ), Braga. ISBN: 978-989-97558-5-7
- Lima A, Teodoro AC, Casimiro JP (2014b) Evaluation of remote sensing data potential in the geological exploration of Freixeda area (Mirandela, Portugal): a preliminary study. Paper presented at the SPIE Remote Sensing. <https://doi.org/10.1117/12.2067183>
- Lotze F (1945) Zur Gliederung der Varisziden der Iberischen Meseta. *Geotekt Forsch* 6:78–92

- Loughlin WP (1991) Principal component analysis for alteration mapping. *Photogramm Eng Remote Sens* 57(9):1163–1169 ISSN: 0099-1112
- Lourenço J, Mateus A, Coke C, Ribeiro A (2002) The Penacova-Régua-Verín Fault Zone in the Telões region (Vila Pouca de Aguiar); some determinant features of its evolution in Late-Variscan times. *Comunicações do Instituto Geológico e Mineiro* 89:105–122
- Mahboob MA, Genc B, Celik T, Ali S, Atif I (2019) Mapping hydrothermal minerals using remotely sensed reflectance spectroscopy data from Landsat. *J South Afr Inst Min Metall* 119(3):279–289. <https://doi.org/10.17159/2411-9717/2019/v119n3a7>
- Manuel R, Brito M, Chichorro M, Rosa C (2017) Remote sensing for mineral exploration in Central Portugal. *Minerals* 7(10):184. <https://doi.org/10.3390/min7100184>
- Martins CB (2005) A exploração mineira romana e a metalurgia do ouro em Portugal. PhD thesis. University of Porto, Porto, Portugal. ISSN: 1647-0745
- Matias R (2004) Ingeniería Minera Romana. In *Elementos de Ingeniería Romana*. Congreso Europeo “Las Obras Públicas Romanas”, Edited by Alba R, Gallo IM, Rodríguez RG. Colegio de Ingenieros Técnicos de Obras Públicas. Tarragona, España. ISBN: 84-688-8190-2
- Mia M, Fujimitsu Y (2012) Mapping hydrothermal altered mineral deposits using Landsat 7 ETM+ image in and around Kuju volcano, Kyushu, Japan. *J Earth Syst Sci* 121(4):1049–1057. <https://doi.org/10.1007/s12040-012-0211-9>
- Mielke C, Bösche N, Rogaß C, Segl K, Gauert C, Kaufmann H (2014) Potential applications of the Sentinel-2 multispectral sensor and the Enmap hyperspectral sensor in mineral exploration. *EARSeL eProceedings* 13(2):93–102. <https://doi.org/10.12760/01-2014-2-07>
- Moradi M, Basiri S, Kananian A, Kabiri K (2014) Fuzzy logic modeling for hydrothermal gold mineralization mapping using geochemical, geological, ASTER imageries and other geo-data, a case study in Central Alborz, Iran. *Earth Sci Inf* 8:197–205. <https://doi.org/10.1007/s12145-014-0151-9>
- Moulton JP, Ridd MK (1990) Integrating remotely sensed data with geophysical data for discrimination of hydrothermally-altered features. 10th Annual International Symposium on Geoscience and Remote Sensing: 2485 - 2488. College Park, Maryland, USA. <https://doi.org/10.1109/IGARSS.1990.688943>
- Murakami T (2006) How is short-wave infrared (SWIR) useful to discrimination and classification of forest types in warm temperate region? *J Forest Plann* 12(2):81–85. https://doi.org/10.20659/jfp.12.2_81
- Mwaniki MW, Moeller MS, Schellmann G (2015) A comparison of Landsat 8 (OLI) and Landsat 7 (ETM+) in mapping geology and visualising lineaments: a case study of central region Kenya. *International Archives of the Photogrammetry. Remote Sens Spat Inform Sci XL-7(W3):897–903*. <https://doi.org/10.5194/isprsarchives-XL-7-W3-897-2015>
- Noronha F, Cathelineau M, Boiron MC, Dória A, Ribeiro M, Nogueira P, Guedes A (2000) A three stage fluid flow model for Variscan gold metallogenesis in northern Portugal. *J Geochem Explor* 71:209–224. [https://doi.org/10.1016/S0375-6742\(00\)00153-9](https://doi.org/10.1016/S0375-6742(00)00153-9)
- Noronha F, Ramos JMF (1993) Mineralizações auríferas primárias no norte de Portugal. *Algumas reflexões Cadernos do Laboratório Xeolóxico de Laxe: Revista de xeoloxía galega e do hercínico peninsular Coruña* 18:133–146 ISSN 0213-4497
- Noronha F, Ribeiro M, Almeida A, Dória A, Guedes A, Lima A, Martins H, Sant’Ovaia H, Nogueira P, Martins T et al. (2013) Jazigos filonianos hidrotermais e aplitopegmatíticos espacialmente associados a granitos (norte de Portugal): 403–438. In *Geologia de Portugal Volume I - Geologia Pré-mesozóica de Portugal*, edited by Rui Dias, Alexandre Araújo, Pedro Terrinha, José Carlos Kullberg, Escolar Editora. ISBN 978-972-592-364-1.
- Pereira B, Azevedo J, Oliveira J, Dias PSA, Leal Gomes C, Carvalho J, Marques A (2012) Contribution of remote sensing to the evidence and location of granite hosted pegmatites—Ponte da Barca (Minho). In MQ Ferreira, MT Barata, FC Lopes, AI Andrade, MH Henriques, R Pena dos Reis, EI Alves (Eds.), *Para Desenvolver a Terra: Memórias e Notícias de Geociências no Espaço Lusófono* (pp. 235-244): Imprensa da Universidade de Coimbra. <http://hdl.handle.net/1822/30031>
- Porwal AK, Kreuzer OP (2010) Introduction to the special issue: mineral prospectivity analysis and quantitative resource estimation. *Ore Geol Rev* 38(3):121–127. <https://doi.org/10.1016/j.oregeorev.2010.06.002>
- Pour A, Hashim M (2015) Hydrothermal alteration mapping using Landsat 8 data, Sar Cheshmeh copper mining district, SE Iran. *J Taibah Univ Sci* 9(2):155–166. <https://doi.org/10.1016/j.jtusci.2014.11.008>
- Pour AB, Park Y, Park TS, Hong JK, Hashim M, Woo J, Ayoobi I (2018a) Evaluation of ICA and CEM algorithms with Landsat-8/ASTER data for geological mapping in inaccessible regions. *Geocarto Int* 34(7):785–816. <https://doi.org/10.1080/10106049.2018.1434684>
- Pour AB, Park TS, Park Y, Hong JK, Zoheir B, Pradhan B, Ayoobi I, Hashim M (2018b) Application of multi-sensor satellite data for exploration of Zn-Pb sulfide mineralization in the Franklinian Basin, North Greenland. *Remote Sens* 10:1186. <https://doi.org/10.3390/rs10081186>
- Pour AB, Park T-YS, Park Y, Hong JK, Muslim AM, Läufer A, Crispini L, Pradhan B, Zoheir B, Rahmani O, Hashim M, Hossain MS (2019) Landsat-8, advanced spaceborne thermal emission and reflection radiometer, and WorldView-3 multispectral satellite imagery for prospecting copper-gold mineralization in the northeastern Inglefield Mobile Belt (IMB), northwest Greenland. *Remote Sens* 11(20):2430. <https://doi.org/10.3390/rs11202430>
- Rajesh HM (2004) Application of remote sensing and GIS in mineral: resource mapping-an overview. *J Mineral Petrol Sci* 99(3):83–103. <https://doi.org/10.2465/jmps.99.83>
- Ribeiro MA, Martins HC, Almeida A, Noronha F (2000) Carta Geológica de Portugal, escala 1:50 000, 6-C (Cabeceiras de Basto), Notícia Explicativa. *Serviços Geológicos de Portugal*, 48.
- Ribeiro A, Marcos A, Pereira E, Llana-Funez S, Farias P, Fernández FJ, Fonseca P, Chaminé H, Rosas F (2003) 3-D strain distribution in the Ibero-Armorican arc : a review. *Ciências da Terra, Universidade de Lisboa* 5:63–64
- Ribeiro A, Munhá J, Dias R, Mateus A, Pereira E, Ribeiro L, Fonseca P, Araújo A, Oliveira T, Romão J, Chaminé H, Coke C, Pedro J (2007) Geodynamic evolution of the SW Europe Variscides. *Tectonics* 26: 1–24. <https://doi.org/10.1029/2006TC002058>
- Ridwan MA, Radzi N, Ahmad W, Mustafa I, Din N, Jalil Y, Isa A, Othman N, Zaki W (2018) Applications of Landsat-8 data: a survey. *Int J Eng Technol* 7(4.35):436–441. <https://doi.org/10.14419/ijet.v7i4.35.22858>
- Robert F, Brommecker R, Bourne B, Dobak PJ, Mcewan C, Rowe RR, Zhou X (2007) Models and exploration methods for major gold deposit types. *Proceedings of Exploration 07: Fifth Decennial International Conference on Mineral Exploration*, 691–711.
- Rowan LC, Goetz AFH, Ashley RP (1977) Discrimination of hydrothermal altered and unaltered rocks in visible and near infrared multispectral images. *Geophysics* 42:522–535. <https://doi.org/10.1190/1.1440723>
- Sabins F (1999) Remote sensing for mineral exploration. *Ore Geol Rev* 14:157–183. [https://doi.org/10.1016/S0169-1368\(99\)00007-4](https://doi.org/10.1016/S0169-1368(99)00007-4)
- Safari M, Maghsoudi A, Pour A (2017) Application of Landsat-8 and ASTER satellite remote sensing data for Porphyry copper exploration: a case study from Shahr-e-Babak, Kerman, south of Iran. *Geocarto Int* 1–42. <https://doi.org/10.1080/10106049.2017.1334834>

- Salisbury JW, Walter LS, Vergo N (1989) Availability of a library of infrared (2.1–25.0 μm) mineral spectra. *Am Mineral* 74:938–939 ISSN: 0003-004X
- Sekandari M, Masoumi I, Pour AB, Muslim MA, Rahmani O, Hashim M, Zoheir B, Pradhan B, Misra A, Aminpour SM (2020) Application of Landsat-8, Sentinel-2, ASTER and WorldView-3 spectral imagery for exploration of carbonate-hosted Pb-Zn deposits in the Central Iranian Terrane (CIT). *Remote Sens* 12:1239. <https://doi.org/10.3390/rs12081239>
- Singh A, Harrison A (1985) Standardized principal components. *Int J Remote Sens* 6:883–896. <https://doi.org/10.1080/01431168508948511>
- Takodjou Wambo JD, Pour AB, Ganno S, Asimow PD, Zoheir B, Reis Salles RD, Nzenti JP, Pradhan B, Muslim AM (2020) Identifying high potential zones of gold mineralization in a sub-tropical region using Landsat-8 and ASTER remote sensing data: a case study of the Ngoura-Colomines goldfield, eastern Cameroon. *Ore Geol Rev* 122: 103530. <https://doi.org/10.1016/j.oregeorev.2020.103530>
- Traore M, Takodjou Wambo JD, Ndepete CP, Tekin S, Pour AB, Muslim MA (2020) Lithological and alteration mineral mapping for alluvial gold exploration in the south east of Birao area, Central African Republic using Landsat-8 Operational Land Imager (OLI) data. *J Afr Earth Sci* 170:103933. <https://doi.org/10.1016/j.jafrearsci.2020.103933>
- USGS (2012) Landsat-a global land-imaging mission: U.S. Geological Survey Fact Sheet 2012. 3072, 4 p. (Revised July 19, 2012). <https://pubs.usgs.gov/fs/2012/3072/>
- USGS (2020a) Landsat 8 (L8) data users handbook. 114. Using the USGS Landsat Level-1 data Product. Available online: <https://www.usgs.gov/land-resources/nli/landsat/using-usgs-landsat-level-1-data-product>. Accessed March 2020
- USGS (2020b) Using the USGS Landsat level-1 data product. Available online: <https://www.usgs.gov/land-resources/nli/landsat/using-usgs-landsat-level-1-data-product>. Accessed March 2020
- van der Meer FD, van der Werff HMA, van Ruitenbeek FJA, Hecker CA, Bakker WH, Noomen MF, van der Meijde M, Carranza EJM, Smeth JB, Woldai T (2012) Multi- and hyperspectral geologic remote sensing: a review. *Int J Appl Earth Obs Geoinf* 14:112–128. <https://doi.org/10.1016/j.jag.2011.08.002>
- Xiang J, Xiao K, Carranza EJM, Chen J, Li S (2020) 3D Mineral prospectivity mapping with random forests: a case study of Tongling, Anhui, China. *Nat Resour Res* 29(1):395–414. <https://doi.org/10.1007/s11053-019-09578-2>
- Zoheir B, Emam A (2012) Integrating geologic and satellite imagery data for high-resolution mapping and gold exploration targets in the South Eastern Desert, Egypt. *J Afr Earth Sci* 66–67:22–34. <https://doi.org/10.1016/j.jafrearsci.2012.02.007>
- Zoheir B, El-Wahed MA, Pour AB, Abdelnasser A (2019) Orogenic gold in transpression and transtension zones: field and remote sensing studies of the Barramiya–Mueilha Sector, Egypt. *Remote Sens* 11: 21–22. <https://doi.org/10.3390/rs11182122>